SLU JST
Sule Lamido University Journal of Science & Technology Vol. 7 No. 1 [June, 2023], pp. 10-27
https://doi.org/10.56471/slujst.v7i.234
Online ISSN: 2736-0903
Print ISSN: 2736-089X
www.slujst.edu.ng

Propagation of Viscoplastic Surges over Complex Topographies

Faisal Balarabe[1,2,*], Usman Haladu Garba[2] and Musa Alhaji Ibrahim[2]
[1]French National Institute for Food, Agriculture and Environment (INRAE), Grenoble, France
[2]Department of Mechanical Engineering, Kano University of Science and Technology, Wudil, Nigeria
[*]faisalbalarabe@kustwudil.edu.ng

[*]Corresponding Author

Abstract

This paper presents an experimental study of a dam break configuration in which free surface of a viscoplastic fluid deposited on a complex 3D topography was tracked and measured. Due to the coexistence in the flows of fluid and solid zones, whose respective boundaries are unknown, simulating the propagation and deposition of free-surface viscoplastic surges remains challenging especially when the topography is complex. The main goal of this study is to perform a well-controlled laboratory experiment which could lead to the recovery of local height of the material deposited on the free surface of the topography through monitoring the propagation of the surges. When the viscoplastic material is deposited on the topography after it reaches an arrested state, an innovative stereoscopy technique (fringe projection) was used. The fringe projection technique is applied to collect the raw data in form of images for further processing. This technique has been commonly used to generate 3D surface information. It simply consists of a video projector projecting a sinusoidal fringe pattern on a surface and a camera-taking image of the surface for further post-procession. The data collected from the experiment was post-treated sequentially as follows; shadow masking, phase shifting, phase unwrapping, filtering and determination of the actual phase signal using Python codes. The actual height of the topography was accurately recovered when two reference surfaces were considered (i.e., the reference plate and the naked topography). In each case, the material is deposited on the topography and their height profiles were plotted. This method allowed us to accurately compute and compare the local height profiles. The two profiles were found to be completely superimposed which turns out that the agreement between these two ways of computing the deposits is excellent. Furthermore, when the experimental height profile has been examined critically, a deviation of 2-2.3mm and 0.48mm were recorded on the upper and lower part of the topography respectively.

Keywords: *Viscoplastic surges, complex topographies, Rheology, Natural hazards, Fringe projection technique, Numerical simulation, Experiment*

1. Introduction

The implementation of dam break configuration received great attention over many years with particular interest devoted to free surface profile such as flow thickness and local height. This is synonymous to the propagation of viscoplastic fluids over vertical obstacles, which has been used in various application to simulate geophysical processes (mudflows, debris flows, etc.). To accurately measure the surge's free surface variations with time, (Cochard & Ancey, 2008) developed a new imaging system consisting of a digital camera coupled with a synchronized micro-mirror projector. This method has been in used until recently the idea of using two projectors had been realized and implemented by (Memetzidou, 2018). Due to the shape of the topography when projecting with only one projector shadows are created, hence the need for two projectors emerges.

Geophysical processes have been defined as gravity-driven mass flows whose dynamical behavior is similar to that of a non-Newtonian fluid. These flows compose naturally a mixture of water, clay, silt and often coarser material such as gravel and boulders (Blasio, 2010). They may also contain trees and human artifact. These types of flows are considered as natural hazards which cause a lot of irreparable damage in the ecosystem e.g., loss

Online ISSN: 2736-0903
Print ISSN: 2736-089X
www.slujst.edu.ng

of lives, destruction of soil fertility and limitation of habitation. This makes it necessary and very important to acquire accurate experimental data in order to assess the predictive capabilities of the existing models. However, looking at this study which has its origin as the implementation of dam break problem for a viscoplastic material over an inclined complex 3D topography, it becomes paramount to design an appropriate experimental protocol that would lead to achieving a better result.

Many researches have been carried out and some are still going on just to provide a qualitative and quantitative estimate of flow velocity, run-out distances and exerted forces/pressures. Particles concentrations and rheological behavior are important for the point of view of physical understanding of the processes, and are important ingredients for the development of accurate models of geophysical processes. Viscoplastic materials are capable of maintaining a proper shape even when resting on a flat area, if the state of the stress in the fluid does not exceed a certain limit (Coussot, 2014).

The basic rheological characteristics of a fluid is its viscosity, which is the ratio of the shear stress and the shear rate (Coussot, 2014). Non-Newtonian fluids differ from Newtonian because the viscosity can change depending on the intensity of the applied stress and/or the length of time that stress is applied, example of viscoplastic fluids is; custard, honey, toothpaste and starch. The behavior of viscoplastic materials is uniquely characterized based on the property known as yield stress. Yield stress fluids possess a transition behavior that makes it possible for them to behave as liquid and sometimes as solid. When they are at rest, they behave like solid but when they are stressed beyond the yield stress, they flow. The yield stress quantifies the stress that the fluid experiences before it yields and begins to flow (Coussot, 2014). This phenomenon is described by Herschel–Bulkley model. The yield stress of the viscoplastic fluid is found at the shear stress that corresponds to the critical torque (Kalyon, 2021). The critical torque does not depend on the spacing of the rheometer. An investigation of the internal dynamics of free-surface surges were made by (Chambon et al., 2020), while observing that the correction terms are responsible for disappearing of the unsheared layer in the tip region, leading-order approximation satisfactorily accounts for the global dynamics of the flow.

Determining the rheological behavior of geophysical materials remain difficult because they encompass coarse and irregular particles over a wide range of size (Ancey, 2007). This is why the actual characteristics of geophysical processes is still a challenging research area. In addition, the description of geophysical flows based on fluid mechanics is a difficult and challenging task, not only because the rheological properties are insufficiently known, but because their behavior may change radically and dramatically with time (Blasio, 2010). (Moyers-Gonzalex et al., 2022) investigate the effects that a temperature-dependent rheology has on the spread rate, length of the block and shape of the free surface when the viscoplastic fluid is released on a horizontal or an inclined surface with a flat, a step-up and a step-down topography. The results revealed that for large values of the yield stress, only the outer fraction of the fluid spread outward, the inner fraction remaining unyielded. It was reported by (Hinton & Hogg, 2022) that flows goes deeper upstream of mounds, with amplitude increasing with increasing yield stress. The result further shows the location where maximum thickness is attained for both Newtonian and non-Newtonian fluids.

Moreover, the presence of non-sinusoidal waveforms in the recorded fringe pattern has caused significant phase measurement errors (when phase shifting analysis is employed) and thereby resulting in considerable errors in the measurement of 3D shape of the objects (Gorthi & Rastogi, 2010). The adoption of physics-informed neural network PINN by (Wu, et al, 2022) in simulation of the propagation process of viscoplastic surges caused by landslides revealed that the depth and particle density of water have effects on the landslide surge propagation as the amplitude increases with deeper water and larger particle density respectively.

One of the most challenging problems in the fringe projection technique is to obtain an accurate and unambiguous 3D shape measurement of objects with no or less surface discontinuities or spatially isolated surfaces. The utmost attention is needed because the obtained wrapped phase map through fringe analysis contains true phase discontinuities (i.e., discontinuities in the wrapped phase map that originate from the object surface

Sule Lamido University Journal of Science & Technology Vol. 7 No. 1 [June, 2023], pp. 10-27
https://doi.org/10.56471/slujst.v7i.234
Online ISSN: 2736-0903
Print ISSN: 2736-089X
www.slujst.edu.ng

discontinuities). To overcome this problem several methods were developed, among which are multi-sensitivity-based unwrapping (Zhao et al., 1994). Although, our main concern is not purely on phase unwrapping processes, hence we will adopt the method reviewed from the literature with some modifications for possible improvement. Discontinuous Galerkin method was used by (Fernandez et al, 2023) to solve shallow viscoplastic flow problems. To achieve this, the Bingham model was coupled with the shallow-water equations. In another paper, a multi grid initialization algorithm has been utilized to numerically investigate viscoplastic flows. When compared with the classic single grid method, a significant contribution was recorded (Maazioui et al, 2023).

(Memetzidou, 2018) applied monochromatic fringe projection technique using two projectors concurrently as shown in figure 1a. They were able to successfully create a color channel correction algorithm to treat monochromatic channels. Due to symmetry of the surface, 1D unwrapping method was used for analyzing the projected fringes for plane plates whereas 2D unwrapping method was used for the complex topography. They could not exactly determine the local height accurately on the topography due to noise as seen in figure 1b, even though 2D unwrapping method was used. Hence, this issue needs special attention. They further found that, when using a combined approach in their experiment, an accurate 3D spatial information about the material deposition on the topography was obtained whereas the concurrent approach did not, but rather gave a noisy result which could not enable them record a good spatial information for the approach adopted. Hence, this study involves modifying and testing their method for possible improvement.

To achieve the possible improvement, the following objectives were targeted; to acquire accurate experimental data in order to assess the predictive capabilities of the existing simulation models, to optimize the projector angle in order to achieve accurate local height profile and avoid having the shadows intersecting, to track and measure the free surface of the flow. To compare and validate the results obtained with existing numerical model.

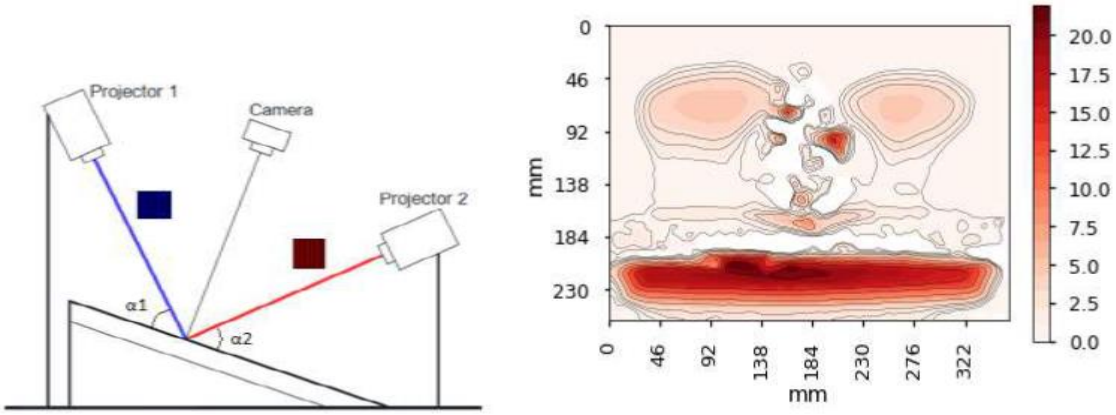

(a) (b)

Figure 1: (a) Fringe projection using two projectors concurrently (b) Morphological representation of local height of material deposited (Memetzidou, 2018).

2. Materials and Methodologies

The topography has dimension 0.40m x 0.40m x 0.10m and has two characteristic obstacles, these are a 3cm height obstacle throughout its width on the upper part and a 10cm height obstacle on the bottom part as shown in figure 2b. The 3D printed topography is placed on a plane which is initially inclined at an angle of 20° with respect to the horizontal axis. This is to enable the fluid once poured and released to flow naturally under the influence of gravitational force.

Sule Lamido University Journal of Science & Technology Vol. 7 No. 1 [June, 2023], pp. 10-27
https://doi.org/10.56471/slujst.v7i.234
Online ISSN: 2736-0903
Print ISSN: 2736-089X
www.slujst.edu.ng

A measured volume of viscoplastic fluid is poured in a box with specific dimension and is suddenly released by lifting it vertically, simulating the dam break problem. As the material reached the arrested state on the lower part of the topography, blue and red images were projected separately and concurrently with sinusoidal fringe pattern using LCD projectors. The fringes projections were done with two projectors. This method of using two projectors is actually novel (not frequently used in previous studies). To further minimize the shadow areas; several calibrations were performed, which is described in the subsequent section. The calibration has conversely revealed that projecting red fringe with upper projector and blue fringe with lower yield better results with minimum shadow areas. However, in this paper we intend to combine the two colors that would help in monitoring the dynamics of the flow. In this case, due to the time constraint, we were unable to successively project 4 images for each color. The free surface is captured using a digital camera and the signal of the projected images was recorded for further image processing and phase analysis in order to track the final deposits on the topography.

The system used in performing this experiment was made up of a metal frame as shown in Figure 2a; the frame is supporting an inclined plane with dimensions 1.10m x 0.60m. The metal frame structure is 2.0m long, 0.60m wide and 1.0m high. This structure also supports the digital camera, which is fixed perpendicular to the inclined surface and it should remain fixed in the position during the experiments. Furthermore, the topography is placed onto the inclined plane and within the camera field of view.

Two projectors are carefully placed at different heights to the two opposite sides of the metal frame, at this point, a lot of attention is needed so they do not move during the experiments. The projection angle is approximately 45° with respect to the inclined plane, for both projectors. The experiment is then commenced when everything is set, we began by projecting sinusoidal fringes with different colors, red for the upper projector and blue for the lower projector. The projectors were used both for the calibration process and for the experiments. The idea of using lower projector for blue fringe and upper projector for red fringe projection has been investigated during preliminary tests. It is expected that a better result would be obtained with this arrangement based on the calibration outcomes.

The system of video projectors used in this experiment was particularly chosen to project periodic color fringes onto the surface of the topography. The digital camera situated above and perpendicular to the topography is to record how the projected fringes are deformed by the free surface of the material. Furthermore, from the deformed fringe pattern, we were able to define equivalence between the local height of the surface and phase offset by using algorithms of signal processing. These are detail in the next subsections.

(a) (b)

Figure 2: (a) Experimental setup (b) Topography

2.1 Theoretical Review

The projectors are setup in order to have 45° projection angle relative to the inclined plane. The digital camera is appropriately set perpendicular to the surface and its parameters such as shutter speed, resolution and

Sule Lamido University Journal of Science & Technology Vol. 7 No. 1 [June, 2023], pp. 10-27
https://doi.org/10.56471/slujst.v7i.234
Online ISSN: 2736-0903
Print ISSN: 2736-089X
www.slujst.edu.ng

aperture number have been accurately chosen to regulate the illumination into the camera. Calibration process: This entails the projection of sinusoidal fringe pattern images with different color for each projector. The process was begun on the reference surface which corresponds to level 0mm and then to plane plates with different heights as presented in fig. 4b. Four images were taken at 0, π/2, π and 3π/2 phase consecutively (i.e., for a phase shift of π/2 for each projector). This technique helped in defining a relation between the phase difference of the signal and the actual height of the plates. This relation enabled us calculate the final height of the material deposited on the topographies. The topography was placed on the inclined plane and sinusoidal images were projected from the two projectors separately. Similarly, four images with the phase shift π/2 for each projector were captured.

A box of viscoplastic fluid of dimensions 6.4cm x 5.4 cm x 19.6 cm (Figure 4c) was placed on the topography. In order to define the rheological parameters of the viscoplastic material used here, three rheometrical tests were performed as presented in table 1 and all the input parameters such as the shear stress, shear rate, temperature and distance between cylinders are controlled from a computer (Chambon et al., 2009). Now, the volume of the viscoplastic material inside the box is monitored and series of experiment were performed. It was ensured that the box was carefully centered on the upper part of the topography. The interface between the box and topography was sealed. The box perpendicular to the surface was then lifted and the fluid was released, simulating the dam break problem.

Table 1: Experimental rheological parameter

Parameters	Test 1	Test 2	Test 3
Temperature ($°C$)	23.8	23.8	23.8
Gap (mm)	1.50	1.50	1.80
Consistency K(Pa.s^n)	2.51	2.66	2.68
Flow index n	0.46	0.46	0.45
Yield stress τ_c (Pa)	2.23	2.45	2.44

The represented data points of the curve correspond to rheometrical test 1. The curve in figure 3 represents the Herschel-Bulkley model determined by fitting the data with corresponding fit parameters $\tau_c = 2.23\ Pa, K = 2.51\ Pa.s^n, n = 0.46$.

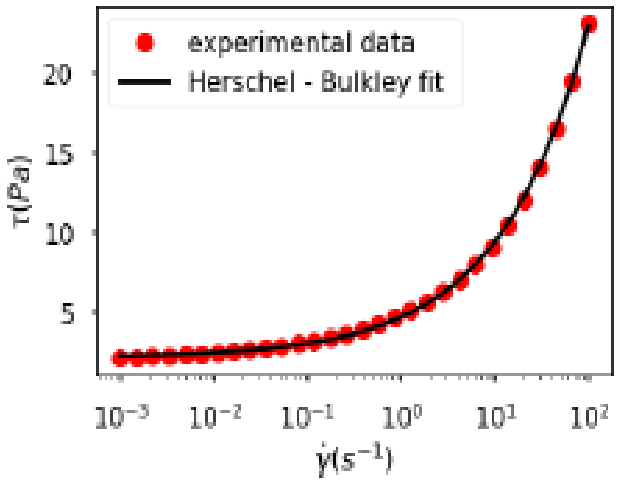

Figure 3: Herschel-Bulkley fit & experimental Steady-state flow curve of Carbopol slurry used in this study: shear stress τ versus shear rate $\dot{\gamma}$ (Memetzidou, 2018).

Once the material has flown and accelerated over the surface of the topography and reached the arrested state (lower part of the topography), four additional sinusoidal fringe images of π/2 phase shift for each projector

Sule Lamido University Journal of Science & Technology Vol. 7 No. 1 [June, 2023], pp. 10-27
https://doi.org/10.56471/slujst.v7i.234
Online ISSN: 2736-0903
Print ISSN: 2736-089X
www.slujst.edu.ng

were captured. The images were taken for post procession using image-processing technique, which enabled determination of the final deposits of the material. The topography was then evacuated and cleaned thoroughly when the image capturing was over.

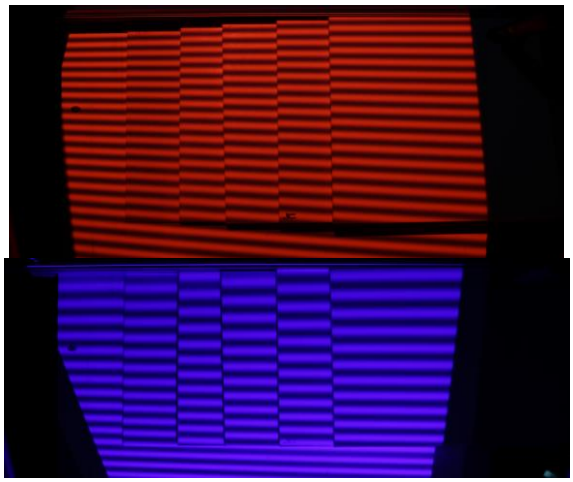

(a)

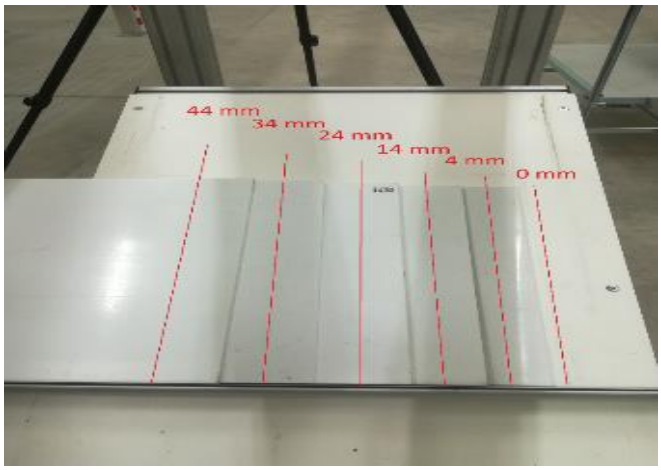

(b)

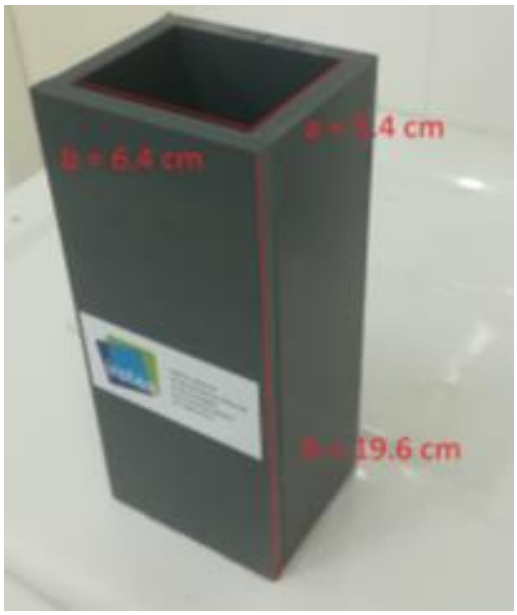

(c)

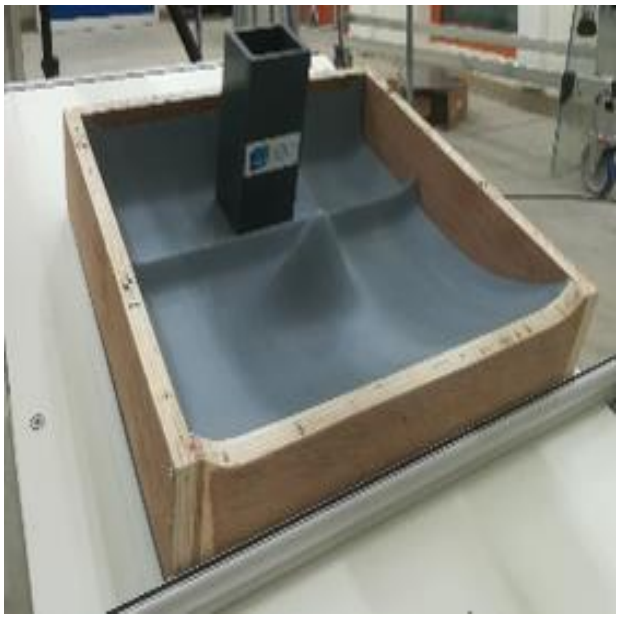

(d)

Figure 4: (a) Calibration plates (b) fringes projection (red and blue fringes)
(c) Experimental box (d) Topographies.

3. Measurement and Post-treatment method

3.1 Fringe Projection Technique

This technique is not a new one as it has been implemented in (Leduc et al., 2014), where the deformed fringes which are generated due to the height difference, provide information about the final height observed because of the material deposited on the surface. As earlier mentioned, the fringe analysis requires that a series of fringes be projected in four different phase shifts viz: 0, $\pi/2$, π and $3\pi/2$ onto the reference plane at the first instance and secondly on the object surface. This process of fringe projection is diagrammatically presented in figure 5 with

Sule Lamido University Journal of Science & Technology Vol. 7 No. 1 [June, 2023], pp. 10-27
https://doi.org/10.56471/slujst.v7i.234
Online ISSN: 2736-0903
Print ISSN: 2736-089X
www.slujst.edu.ng

the two projectors and the camera pointing towards the topographies. Phase unwrapping algorithm was then applied to compute the phase difference between these two surfaces (reference and object surface).

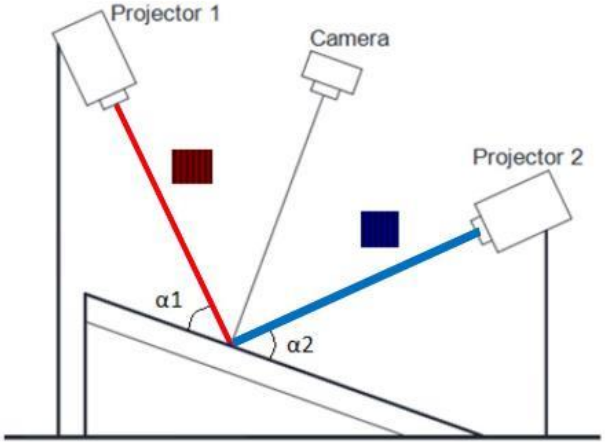

Figure 5: Fringe projection technique

3.2 Shadow Masking

Due to the shape of the topography, when projecting with only one projector, it will be impossible to acquire information in the area covered by the shadow. For this reason, the technique of projecting fringes with both projectors concurrently was adopted which helped us obtained information about the final deposits all over the topographies. Figure 6 shows the shadow areas formed by each projector. These areas intersect only in a limited part and information about the rest of the topography is easily obtained using both projectors. Based on the above, we combined in our final calculations the visible areas of both.

After combining the two colors, we used mask to define the shadow areas and the final height distribution was calculated using the relation below:

$$h = \frac{(mask_{red}h_{red})+(mask_{blue}h_{blue})}{mask_{red}+mask_{blue}} \qquad (1)$$

where $mask_{red}$ corresponds to the masked shadow area for red projection and $mask_{blue}$ for the blue projection. However, h_{red} and h_{blue} correspond to the height distribution obtained for each color separately.

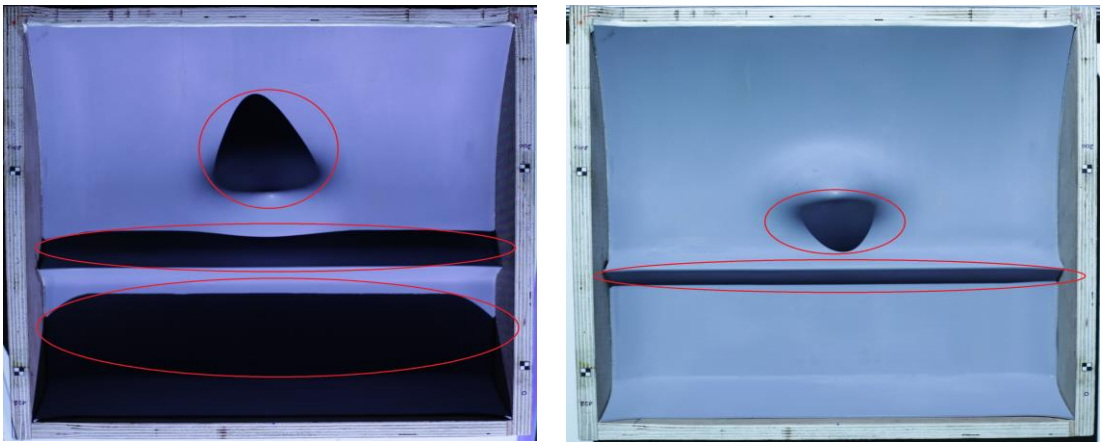

Figure 6: Shadow masking for both upper and lower projector.

SLUJST
Sule Lamido University Journal of Science & Technology Vol. 7 No. 1 [June, 2023], pp. 10-27
https://doi.org/10.56471/slujst.v7i.234
Online ISSN: 2736-0903
Print ISSN: 2736-089X
www.slujst.edu.ng

3.3 Projection Angle and Fringes Frequencies

It is significant to note that due to the surface inclination, the projection angle of the projected fringes does vary for the two projectors. At every time we come to perform the experiment either the calibration or the real experiment, this angle has to be measured and adjusted. Eq. (2) is introduced which describes the relation of all the projection parameters.

$$\Delta\phi = 2\pi f \frac{\Delta h}{tan\alpha} \quad (2)$$

where $\Delta\phi$ is the unwrapped phase difference, f the projected frequency of the fringes, Δh the height difference and α the angle of projection, which also differs for the two projectors. It is the angle formed between the projection direction and the inclination surface. However, choosing the best values for these parameters is also part of the calibration.

3.4 Phase Shifting

Before we proceed on the phase shifting, a highlight on how the phase was measured based on the signal intensity obtained from the reference (I_{ref}) and the deformed surfaces (I_{obj}) is given. If we introduce Eq. (3) and (4) for the intensity of signal projected on the reference surface and the intensity of signal projected on the deformed surface respectively. f being the spatial frequency, A and B are constant parameters for adjustment purposes to avoid saturation of the projected image. Several tests were carried out and finally choose their values as A (150) and B (50) (Memetzidou, 2018).

$$I_{ref} = Acos(2\pi fx) + B \quad (3)$$

Based on the two cases, we firstly consider the inclined plane to be the reference and the plates of different heights as object (calibration method). Secondly, we consider the topography without deposits as reference and the topography covered with material as object (dam break problem activated).

$$I_{ref} = Acos(2\pi fx + \Delta\phi) + B \quad (4)$$

Since $\Delta\phi$ is the signal distortion in Eq. (4), this indicates that the two signal are out of phase. However, it necessitates the use of phase shifting technique in order to recover the phase difference which helped in extracting information about the final height.

The phase shifting method comprises of four projected images with fringe pattern that are out of phase by π/2 as presented in figure 7 and described in the following equations.

$$I_{ref0} = Acos\left(\phi_{ref} + 0\right) + B \quad (5)$$

$$I_{ref1} = Acos\left(\phi_{ref} + \frac{\pi}{2}\right) + B \quad (6)$$

$$I_{ref2} = Acos\left(\phi_{ref} + \pi\right) + B \quad (7)$$

$$I_{ref3} = Acos\left(\phi_{ref} + 3\pi/2\right) + B \quad (8)$$

Where ϕ_{ref} is the phase of reference.

To obtain the phase, Eq. (5) was subtracted from Eq. (7) and arrived at Eq. (9);

$$I_{ref0} - I_{ref2} = cos\left(\phi_{ref} + 0\right) - \cos\left(\phi_{ref} + \pi\right) = 2\cos\left(\phi_{ref}\right) \quad (9)$$

This was followed by subtracting Eq. (6) from Eq. (8) and obtained Eq. (10);

Sule Lamido University Journal of Science & Technology Vol. 7 No. 1 [June, 2023], pp. 10-27
https://doi.org/10.56471/slujst.v7i.234
Online ISSN: 2736-0903
Print ISSN: 2736-089X
www.slujst.edu.ng

$$I_{ref1} - I_{ref3} = cos\left(\phi_{ref} + \frac{3\pi}{2}\right) - \cos\left(\phi_{ref} + \frac{\pi}{2}\right) = 2\sin(\phi_{ref}) \quad (10)$$

Dividing Eq. (10) by Eq. (9), we finally arrived at Eq. (11);

$$\frac{I_{ref1} - I_{ref3}}{I_{ref0} - I_{ref2}} = \frac{2\sin(\phi_{ref})}{2\cos(\phi_{ref})} = \tan(\phi_{ref}) \quad (11)$$

Eq. (11) can further be expressed as;

$$\phi_{ref} = \arctan\left(\frac{I_{ref1} - I_{ref3}}{I_{ref0} - I_{ref2}}\right) \quad (12)$$

Applying the above procedure for the deformed fringes, we were able to express the phase shift of the surface to measure;

$$\phi_{obj} = \arctan\left(\frac{I_{obj1} - I_{obj3}}{I_{obj0} - I_{obj2}}\right) \quad (13)$$

And finally computed the phase difference from Eq. (12) and (13),

$$\Delta\phi = \phi_{obj} - \phi_{ref} \quad (14)$$

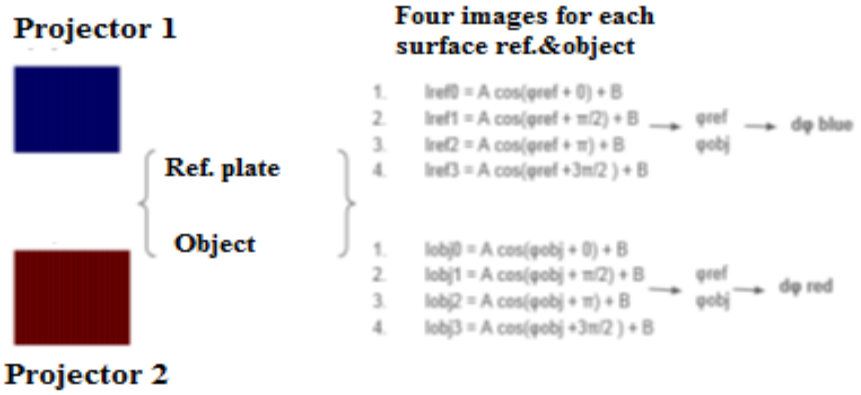

Figure 7: Phase shifting technique for two color fringes.

3.5 Phase Unwrapping

When it comes to phase shifting between two relative surfaces, it become paramount to apply this method because the amplitude of the phase that is obtained can take any value in the domain of real numbers and exceeds the range [-π, +π]. The aim here is that, whenever the phase exceeds this range, it will be unwrapped so that it remains within the usual range [-π, +π]. In such cases, the wrapped phase will contain one or more 2π jumps. The 2π jumps that are present in the wrapped phase signal (Figure 8a) must be remove in order to recover the actual signal that can take any real value and make it usable for further processing (Memetzidou, 2018). Therefore, the essence of performing the phase unwrapping is when the phase value is larger than +π, 2π jumps is subtracted from the wrapped signal. However, when the phase value is smaller than –π, 2π is added to the signal and regains the actual phase signal.

Sule Lamido University Journal of Science & Technology Vol. 7 No. 1 [June, 2023], pp. 10-27
https://doi.org/10.56471/slujst.v7i.234
Online ISSN: 2736-0903
Print ISSN: 2736-089X
www.slujst.edu.ng

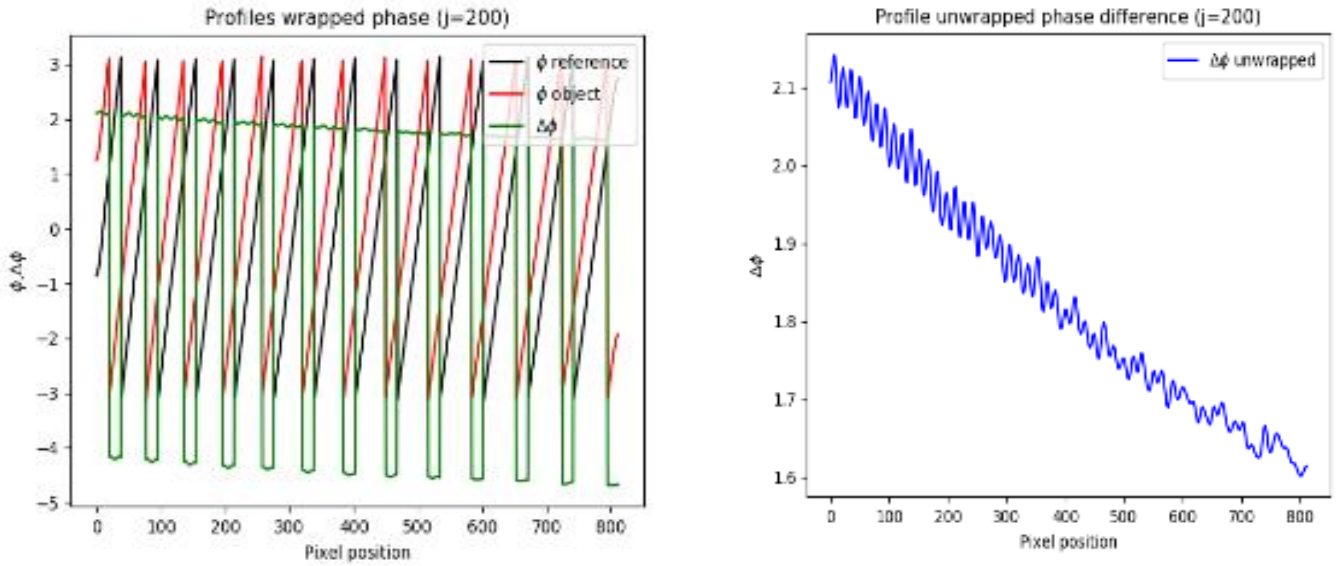

(a) (b)

Figure 8: (a) Wrapped and (b) Unwrapped phase difference.

Figure 8a depicts the profiles of the wrapped phase signal for the calibration plate placed on the inclined plane. It became paramount to unwrap this signal in order to minimize the presence of shadows, fringe discontinuities and noise. Figure 8b represents the unwrapped phase signal with no discontinuities and minimum noise. The function used to achieve all these post-treatment processes were obtained from python skimage library.

3.6 Principles of Filtering the Phase Signal

This principle has been applied to get rid of all the noises presence in the phase signal. The idea of using Gaussian filter arises because of its advantages over other filters and its ability to blur image and reduces noise without affecting the linearity of the system, hence it is a linear filter. It helped in smoothing noise on the images by reducing contrast and enabling edge detection.

The Gaussian filter works by using 2D distribution as point spread function. It is achieved by applying convolution to the 2D Gaussian distribution function with the image. Gaussian kernel is separable, which allows fast computation, even though it might not preserve image brightness (Davies, 2005).

3.7 Principles of Calibration Plates

As earlier described that fringe projection technique was used to determine a relation connecting the phase difference $\Delta\phi$ and the height difference Δh, which can be expressed generally in Eq. (15);

$$\Delta h = f(\Delta\phi) \qquad (15)$$

Having obtained the unwrapped $\Delta\phi$ for the entire surfaces of the plates, the vertical $\Delta\phi$ profiles corresponding to each plate and subsequently to each height was defined. This made it possible to develop a relation between each $\Delta\phi$ with each height h (mm). The profiles of each height are represented by curves with increasing or decreasing linear trends as depicted in figure 9. To determine the local calibration parameters, linear fitting was applied.

The linear fitting is applied at each pixel of the image to recover the coefficient a(x, y). Inverting the calibration relation to recover height values from phase differences $\Delta\phi$. It is mathematically represented by Eq.

Sule Lamido University Journal of Science & Technology Vol. 7 No. 1 [June, 2023], pp. 10-27
https://doi.org/10.56471/slujst.v7i.234
Online ISSN: 2736-0903
Print ISSN: 2736-089X
www.slujst.edu.ng

(16). Knowing that a(x, y) coefficient contains information about each height. Figure 9, depicts the plots that represents the relation between a(x, y) and the various known heights (0, 4, 14, 24, 34, 44 mm) respectively. By assuming zero intercept and applying the linear fitting to these five points (orange line), we also assumed a linear relation between a(x, y) coefficient and the heights. Two additional coefficients were stem out as a_1 and a_2 as expressed in Eq. (17).

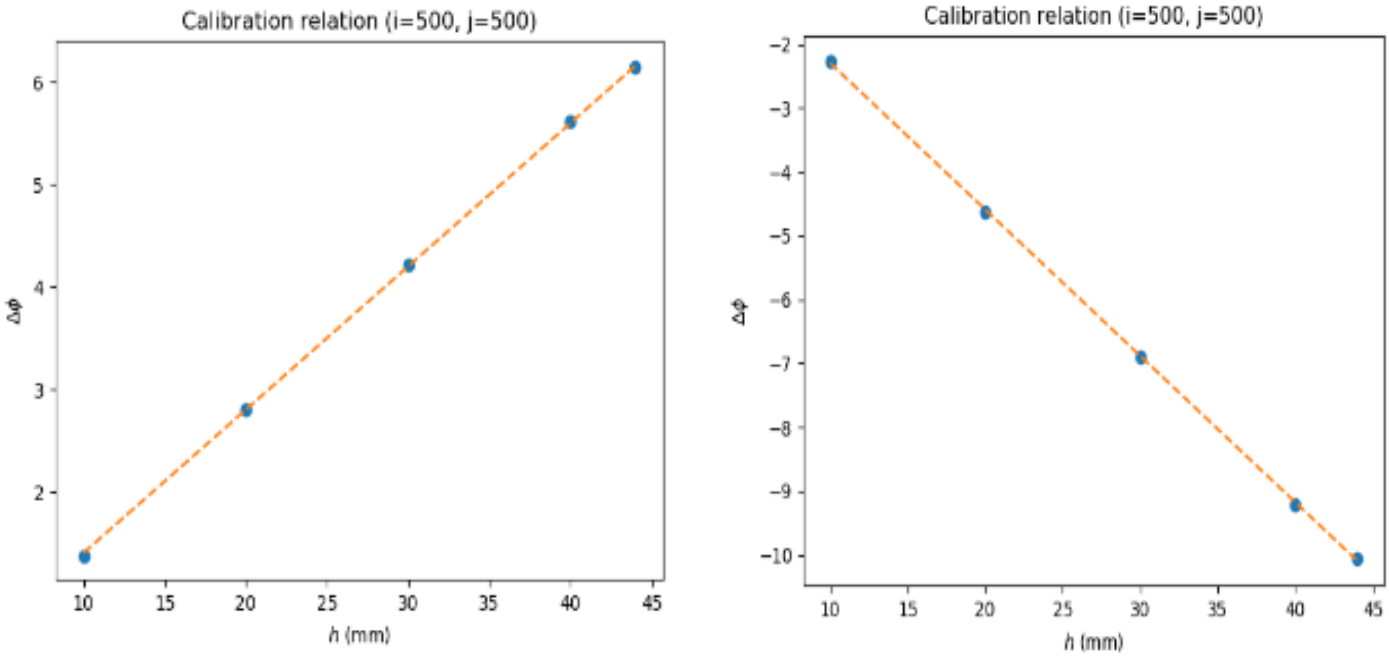

Figure 9: calibration coefficient a (x, y)

$$\Delta\phi = a(x,y)h \quad (16)$$

$$a(x,y) = a_1 x + a_2 \quad (17)$$

Combining Eq. (16) and (17), we get,

$$\Delta\phi = (a_1 x + a_2)h \quad (18)$$

Expressing equation 18 in term of $h(\phi, x)$

$$h(\phi, x) = \frac{\Delta\phi}{a_1 x + a_2} \quad (19)$$

Eq. (19) represents the calibration relation that links $\Delta\phi$ with h. Applying this equation to the data obtained will lead to the corrected heights of the calibration plates. Upon performing the real experiment, this equation was used to acquire the actual final heights of the material deposited.

4. Results

4.1 Results of Topography Height without Deposits

The result presented in figure 10, is that of actual height of the topography without material deposited on it when a 10mm plate was considered as reference plate and the topography as the object. The experimental height fields were computed as shown in figure 10a. However, figure 10b is the theoretical height fields, which is a known height fields from which the real topography was actually generated from its data through 3D printing. At pixel

Sule Lamido University Journal of Science & Technology Vol. 7 No. 1 [June, 2023], pp. 10-27
https://doi.org/10.56471/slujst.v7i.234
Online ISSN: 2736-0903
Print ISSN: 2736-089X
www.slujst.edu.ng

position along x-axis which corresponds to (j = 200) on the topography, the height profiles for red and blue are presented while for their combination at (j = 230) as shown in figure 11. Getting these profiles enabled us know what we exactly needed to subtract when material is deposited on the topography to recover its local height. The yellowish portion at the mid of the figure is representing the area where the peak topography is situated with the protruded little white as the part of shadows that have been masked.

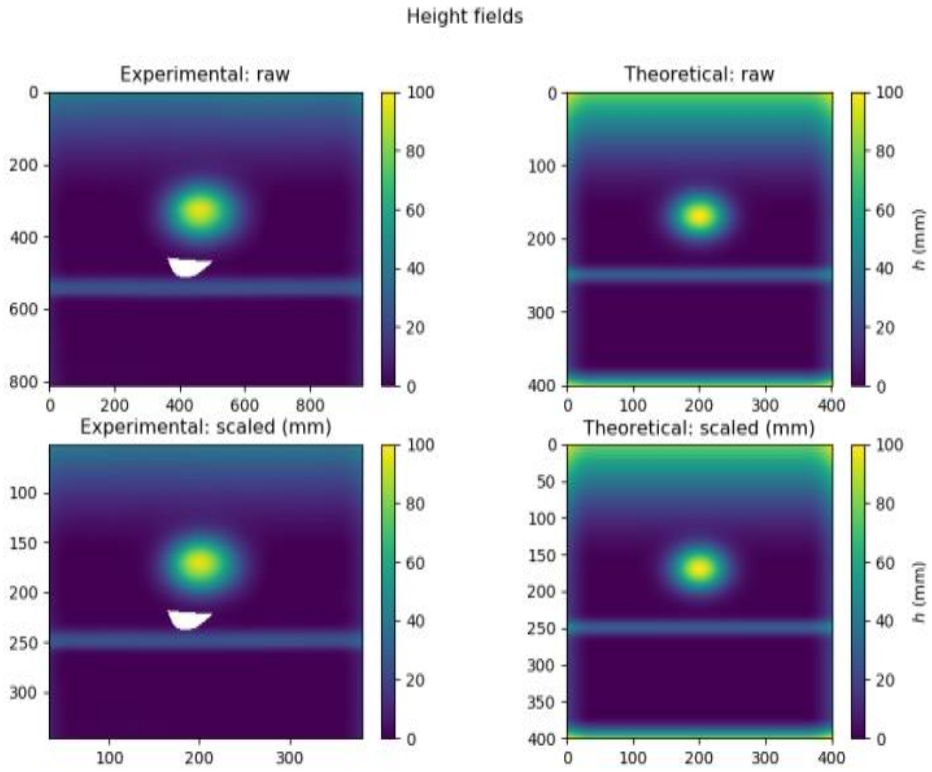

Figure 10: Topography height distribution (Experimental and Theoretical)

In Figure 11, the vertical profiles were plotted at 200 pixels for experimental and theoretical model each. Since we want to show the difference between the two that is why the profiles were plotted at the same pixels position and because the largest deposit is around that region. Figure 11a and b correspond to experimental blue and red projection respectively, while 11c is the combined (red and blue) projection. The maximum peak is around (h = 60mm) which sloped down to the lowest level on the topography and raised after some few pixels (say 200 pixels) to (h = 40mm). This is to accurately portray dam break configuration. In figure 11a & b, the breakage around (500 – 600 pixels) represents the area covered by shadow and which cannot be well captured. When the two colors are combined, we have captured a smooth superimposed trend as shown in Figure 11c.

Sule Lamido University Journal of Science & Technology Vol. 7 No. 1 [June, 2023], pp. 10-27
https://doi.org/10.56471/slujst.v7i.234
Online ISSN: 2736-0903
Print ISSN: 2736-089X
www.slujst.edu.ng

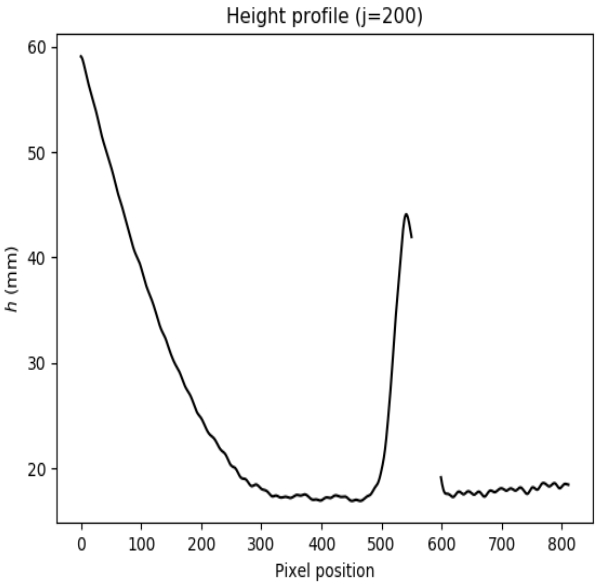

(a) Blue Projection (Experimental)

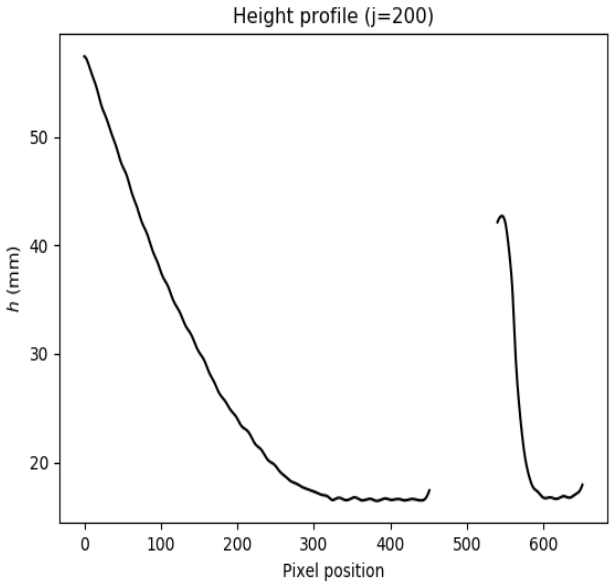

(b) Red Projection (Experimental)

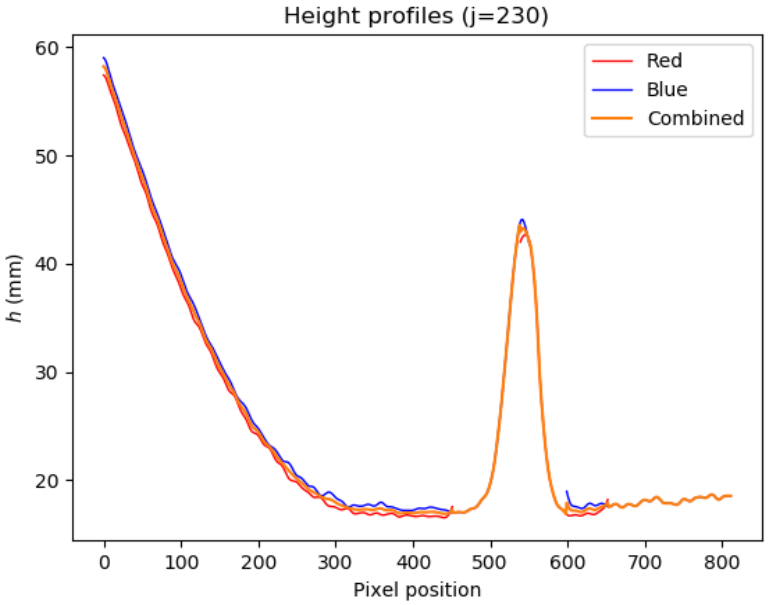

(c) Combined Projection (Experimental)

Figure 11: Topography heights without material deposits for each case

4.2 Results of Topography Height with Deposits using Reference Plate

In Figure 12, we present the result of both experimental and numerical model. The result shows height distribution of the topography when material is deposited on it. In this case, the height distribution has been computed with respect to the reference plate. With experimental raw on the left and theoretical raw on the right of the figure.

Sule Lamido University Journal of Science & Technology Vol. 7 No. 1 [June, 2023], pp. 10-27
https://doi.org/10.56471/slujst.v7i.234
Online ISSN: 2736-0903
Print ISSN: 2736-089X
www.slujst.edu.ng

Furthermore, in an attempt to visualize and acquire an insight of the free surface especially on the part where there is a maximum deposit, the height profile was plotted at a pixel position (200) Figure 13. The discontinuities on the profile are the areas where shadows have been observed, it is found to be large on the red projection. An effort was put in place to mask the areas, projected both fringes separately, and then combined so that we can easily get information on these shadow areas.

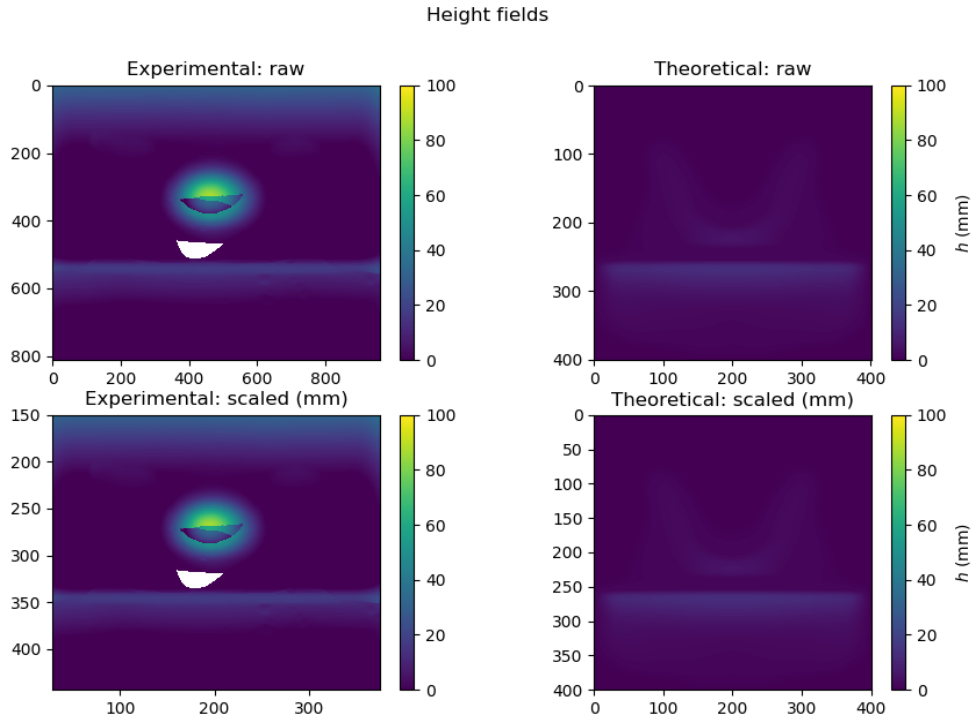

Figure 12: Topography height distribution with deposits (Experimental and Theoretical)

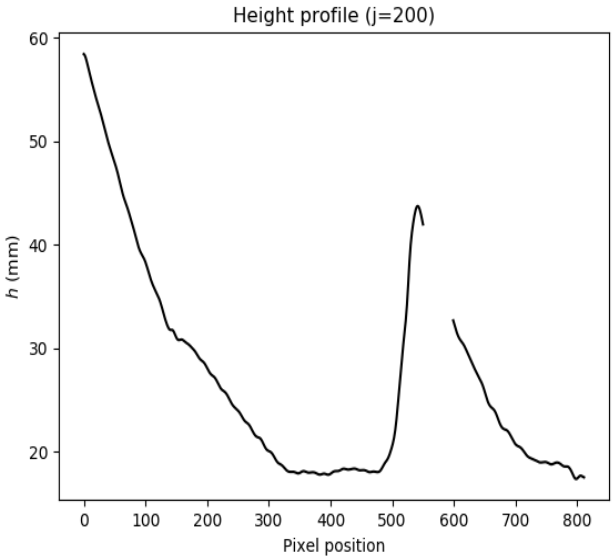

(a) Blue Projection (Experimental)

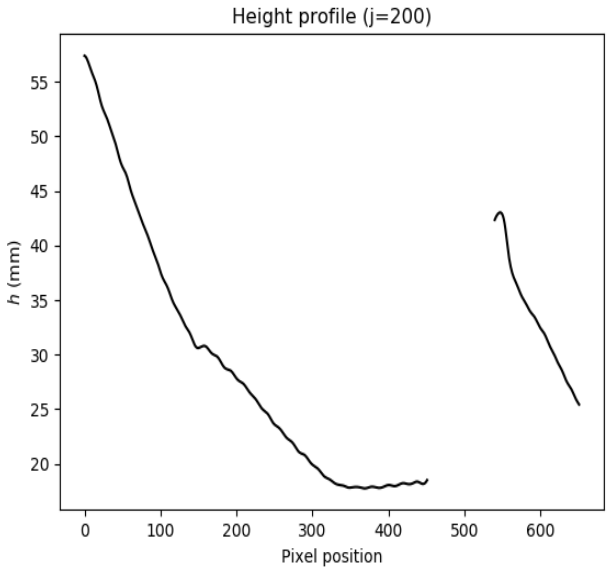

(b) Red Projection (Experimental)

Sule Lamido University Journal of Science & Technology Vol. 7 No. 1 [June, 2023], pp. 10-27
https://doi.org/10.56471/slujst.v7i.234
Online ISSN: 2736-0903
Print ISSN: 2736-089X
www.slujst.edu.ng

Figure 13: Vertical profiles for experimental topography height with deposits

4.3 Results obtained using Naked Topography as Reference

Figure 14a describes the typical morphological distribution of the viscoplastic material deposited over the topography after arrested state has been reached and Figure 14b shows the vertical height profiles for combined approach (i. e when both blue and red projection are combined). Figure. 14c shows a comparison between the method used in generating the results in the previous section and the one used in computing the results in this section. The former used reference plate as reference surface while the latter used naked topography as reference surface. Figure 14b shows that more material was deposited at the lower part of the topography with maximum local height (h = 15mm) between (600 – 700 pixels). The material deposited at the upper part of the topography was up to (h = 5mm) and which falls between (200 – 300 pixels).

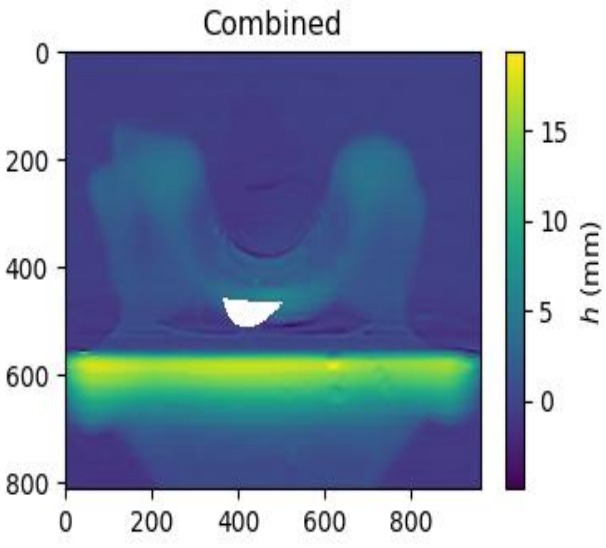

(a) Topography with Material Deposits

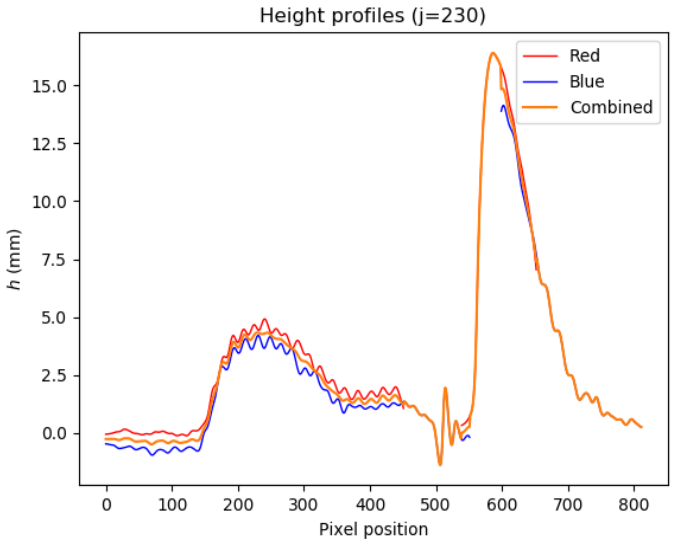

(b) Vertical Profiles for Combined Approach

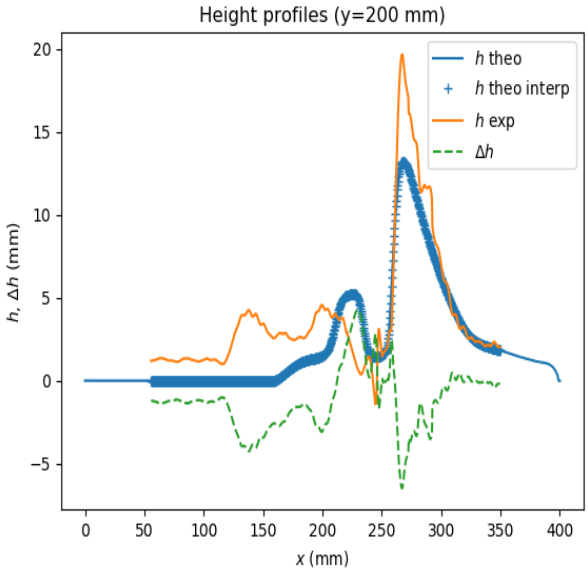

(c) Naked Topology as Reference Surface

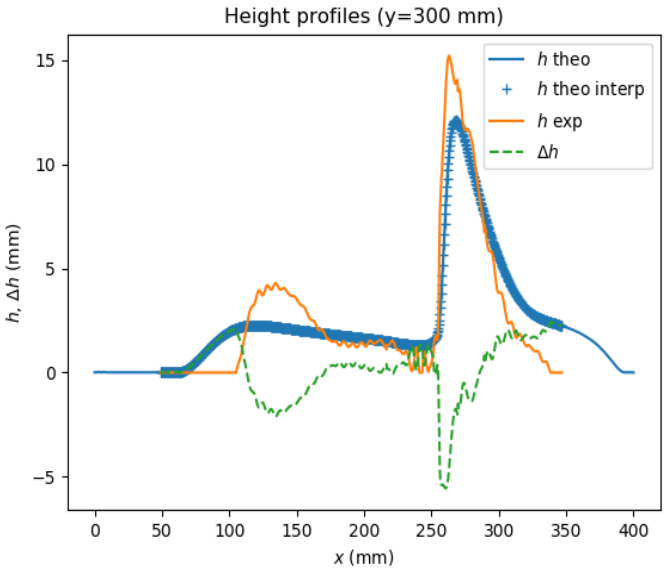

(d) Reference Plate as Reference Surface

Sule Lamido University Journal of Science & Technology Vol. 7 No. 1 [June, 2023], pp. 10-27
https://doi.org/10.56471/slujst.v7i.234
Online ISSN: 2736-0903
Print ISSN: 2736-089X
www.slujst.edu.ng

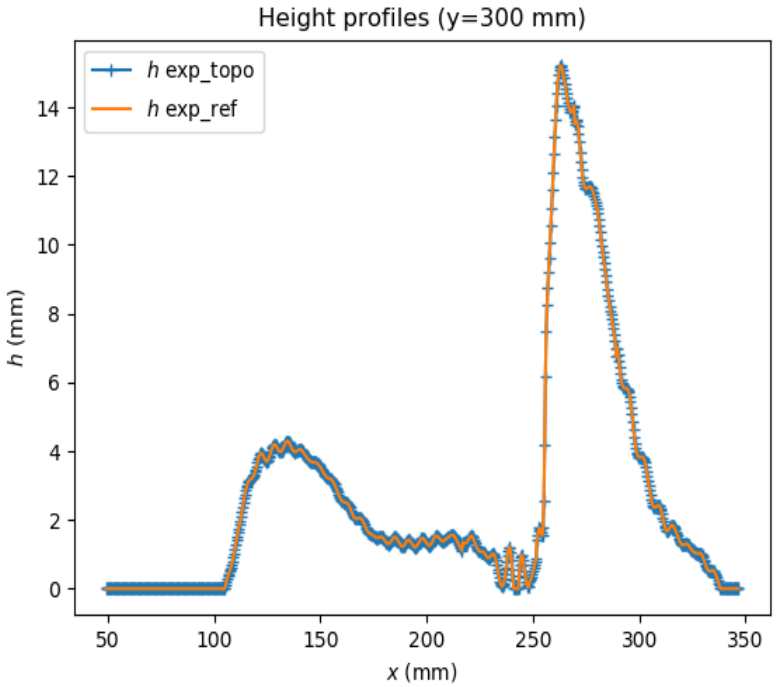

(e) Superimposed Results for the Two References Considered

Figure 14: Results comparing the two references (naked topography and reference plate), morphology of the deposits and their height distribution in each case.

5. Discussion

The morphological representation of material deposited on the topography in Figure 14a has shown that the upper part of the topography has more material concentration due to the nature of the obstacle. However, in the bottom part of the topography, we can see some deposits that are almost symmetric. To be able to directly investigate the differences between the two reference surfaces (reference plate and naked topography), the results obtained are compared, and the naked topography is subtracted.

Figure 14b shows vertical profiles for concurrent projection. With this method, we were able to drastically reduce the shadows, which lead to improvement in the information acquired. It is obvious that there is still some portion with noise, which may affect our results in one way or the other. As depicted in Figure 14c and 14d, We can also observe that on the upper part of the topography, there is height variation of about 2 - 2.3 mm whereas the deviation on the lower part is around 0.48mm which can be considered negligible. This is quite possible, because the discrepancies could be attributed to the presence of the visible little shadow on the upper part of the topography. Similarly, it is obvious that on the lower part, we observed very little height variations, which might be due to some unavoidable noise presence.

Figure 14e has shown that when the naked topography has been subtracted from the two cases considered the two profiles are completely superimposed. It turns out that the agreement between these two ways of calculating the deposits is actually excellent.

It can be observed in figure 11a & 11b that some discontinuities are seen in between 500 – 600 pixels. This correspond to the portion in which the material deposited are not captured due to shadow with single projection (either red or blue projection alone). However, with the help of combining the two projections, an

Online ISSN: 2736-0903
Print ISSN: 2736-089X
www.slujst.edu.ng

accurate information about the material deposited were obtained as seen in Figure 11c and 14b. looking at the local height profiles presented in figure 11, 13, & 14 show that more material was deposited at the upper part of the topographies due to the rheological property of the viscoplastic fluid. The graphs obtained have the same trends as the Herschel-Bulkley fit (Figure 3). Moreover, because of the inability of the fluid to flow under lesser stress (gravity driven in this case), we have noted a higher trend at the beginning (i.e., upper part) and lower flow thickness at the lower part. The heights variation is translated to the non-linearity of the curve and which obeys the law of non-Newtonian fluid and hence agreed with the existing numerical model.

6. Conclusion

The implementation of video projection method allowed us to track and measure how non-Newtonian fluid (viscoplastic) spread over the free surface of a complex 3D topography. The method leads us to revalidation of the existing numerical model. It has come to conclusion that the combined approach is more effective than the separate color projection because it actually helps to reduce the extent of zones that are not visible due to shadows. More so, it can be deduced that when viscoplastic fluid is released over complex topography, more materials are concentrated on the upper part of the topography and formed almost a symmetric deposit on the bottom part. The discrepancies recorded are a promising value when compared with that of the literature. The methods adopted in calculating the deposits are superb because there is good agreement between them

Acknowledgement

The authors would like to express their utmost gratitude to the French National Institute for Food, Agriculture and Environment (INRAE) and TEC21 Grenoble, France for their technical advice, guidance and support for this study.

References

Ancey, C. (2007). Plasticity and geophysical flows: a review in Journal of Non- Newtonian Fluid Mechanics 142.1-3, pp. 4–35.

Blasio, F. V (2010). Introduction to the physics of Landslides “Lecture notes on the Dynamics of Mass Wasting”. ISBN 978-94-007-1121-1. Springer Science Media Publication.

Chambon, G., Freydier, P., Naaim, M. and Vila, J.-P. (2020). Asymptotic expansion of the velocity field within the front of viscoplastic surges: comparison with experiments. Journal of Fluid Mechanics, vol. 884, A43. doi:10.1017/jfm.2019.943.

Chambon, G., Ghemmour, A. and Laigle, D. (2009). Gravity-driven surges of a viscoplastic fluid: An experimental study. In: Journal of Non-Newtonian Fluid Mechanics 158.1-3, pp. 54–62.

Cochard, S. and Ancey, C. (2008). Tracking the free surface of time-dependent flows: image processing for the dam-break problem. 44.1, pp. 59–71.

Coussot, P. (2014). Rheophysics Laboratoire Navier Université Paris-Est Champs-Marne, France. ISBN 978-3-319-06148-1, Springer international publishing Switzerland.

Davies, E. R., (2005). Chapter three: Basic Image Filtering Operations in Signal Procession and its Application, Machine Vision (Third Edition), Published in Elsevier. ISBN 9780122060939, https://doi.org/10.1016/B978-012206093-9/50006-X. Pages 47-101.

Fernandez, F., Lopez, S. and Gonzalez-Andrade, S. (2023). Regularized approach for Bingham viscoplastic shallow flow using the discontinuous Galerkin method. Research gate preprint: https://www.researchgate.net/publication/367462352.

Gorthi, S. S. and Rastogi, P. (2010). Fringe projection techniques: whither we are? In Optics and lasers in engineering 48. IMAC-REVIEW-2009-001, pp. 133–140.

Hinton, E. M. and Hogg, A. J. (2022). Flow of a yield-stress fluid past a topographical feature. Journal of Non-Newtonian Fluid Mechanics,Volume 299, ISSN 0377-0257, https://doi.org/10.1016/j.jnnfm.2021.104696.

Online ISSN: 2736-0903
Print ISSN: 2736-089X
www.slujst.edu.ng

Kalyon, D. M. (2021). Yield stress and other flow and wall slip parameters of viscoplastic fluids from steady torsional flow Research gate Preprint. https://www.researchgate.net/publication/353068031

Maazioui, S., Kissami, I., Benkhaldoun, F. and Ouazar, D. (2023). Numerical study of viscoplastic flows using a multigrid initialization algorithm. Algorithms 16(1), 50. https://doi.org/10.3390/a16010050.

Memetzidou, E. M. (2018). "Propagation of viscoplastic surges over complex topographies" Project report submitted to IRSTEA Laboratoire, Grenoble.

Moyers-Gonzalex, M., Hewett, J. N., Cusack, D. R., Kennedy, B. M. and Sellier, M. (2022). Non-isothermal thin-film flow of a viscoplastic material over topography. Researchsquare.preprints.DOI:https://doi.org/10.21203/rs.3.rs-2019547/v1.

Wu, Y., Shao, K., Piccialli, F. and Mei, G. (2022). Numerical modeling of the propagation process of landslide surge using physics-informed deep learning. Advanced Modeling and Simulation in Engineering Sciences 9:14 https://doi.org/10.1186/s40323-022-00228-6.

Zhao, H., Chen, W. and Tan, Y. (1994). Phase-unwrapping algorithm for the measurement of three-dimensional object shapes, Appl. Opt. 33 (20) 4497–450.